Roh *et al. Energy Mater.* **2025**, *5*, 500128
DOI: 10.20517/energymater.2025.59

Energy Materials

Article

Open Access

Check for updates

Rapid flame induced dual-metal doping on WO_3 electrode for boosting photo-electrochemical water oxidation

Seung Hun Roh[1,#], Jaekyum Kim[1,#], Won So[1], Yuankai Li[1], Won Tae Hong[1], Hyun Min Kwon[1], Sae Byeok Jo[1], Wooseok Yang[1], Byung-Keun Oh[3], Chan-Hwa Chung[1], Jongwook Park[4], Chisung Ahn[5,*], Byung-Hyun Kim[6,7,*], Jung Kyu Kim[1,2,*]

[1]School of Chemical Engineering, Sungkyunkwan University (SKKU), Suwon 16419, Republic of Korea.
[2]SKKU Advanced Institute of Nano Technology (SAINT), Sungkyunkwan University (SKKU), Suwon 16419, Republic of Korea.
[3]Department of Chemical and Biomolecular Engineering, Sogang University, Seoul 04107, Republic of Korea.
[4]Integrated Engineering, Department of Chemical Engineering, Kyung Hee University, Yongin 17104, South Korea.
[5]Heat & Surface Technology R&D Department, Korea Institute of Industrial Technology, Siheung 15014, Republic of Korea.
[6]Department of Chemical and Molecular Engineering, Hanyang University ERICA, Ansan 15588, Republic of Korea.
[7]Department of Applied Chemistry, Center of Bionano Intelligence Education and Research, Hanyang University ERICA, Ansan 15588, Republic of Korea.
[#]Authors contributed equally.

***Correspondence to:** Dr. Chisung Ahn, Heat & Surface Technology R&D Department, Korea Institute of Industrial Technology, 113-58 Seohaean-ro, Siheung 15014, Republic of Korea. E-mail: cahn@kitech.re.kr; Prof. Byung-Hyun Kim, Department of Chemical and Molecular Engineering, Hanyang University ERICA, 55 Hanyangdaehak-ro, Sangnok-gu, Ansan 15588, Republic of Korea. E-mail: bhkim00@hanyang.ac.kr; Prof. Jung Kyu Kim, School of Chemical Engineering, Sungkyunkwan University (SKKU), 2066 Seobu-Ro, Jangan-gu, Suwon 16419, Republic of Korea. E-mail: legkim@skku.edu

How to cite this article: Roh, S. H.; Kim, J.; So, W.; Li, Y.; Hong, W. T.; Kwon, H. M.; Jo, S. B.; Yang, W.; Oh, B. K.; Chung, C. H.; Park, J.; Ahn, C.; Kim, B. H.; Kim, J. K. Rapid flame induced dual-metal doping on WO_3 electrode for boosting photo-electrochemical water oxidation. *Energy Mater.* **2025**, *5*, 500128. https://dx.doi.org/10.20517/energymater.2025.59

Received: 13 Mar 2025 **First Decision:** 24 Apr 2025 **Revised:** 12 May 2025 **Accepted:** 27 May 2025 **Published:** 26 Jun 2025

Academic Editor: Yuhui Chen **Copy Editor:** Fangling Lan **Production Editor:** Fangling Lan

Abstract

A bidirectional co-doping of transition metal Fe and post-transition metal Sn on WO_3 photoanode *via* a facile one step flame-doping process demonstrates the challenging amelioration of both thermodynamic charge migration and surface catalytic kinetics, achieving high-efficient photoelectrochemical (PEC) water oxidation reaction in a neutral pH. The direct flamethrower with rapid thermal flux effectively induces the bidirectional doping of Fe^{3+} and Sn^{4+} into WO_3 without damaging its nanostructure and fluorine-doped tin oxide glass substrate. From the synergetic effect of the dual-metal doping, the photoinduced charge migration and the surface water oxidation kinetics are effectively ameliorated. As a result, the Fe/Sn co-doped WO_3 photoanode shows significantly

enhanced PEC response with 6.16-fold higher photocurrent density performance at 1.23 V_{RHE} than bare WO_3. This work highlights the facile metal atom co-doping method without affecting intrinsic properties of photoanode and substrate for boosting the PEC water splitting performance and solar fuel production.

Keywords: Flame treatment, dual metal co-doping, oxygen evolution reaction, photoelectrochemical reaction, water splitting

INTRODUCTION

As a promising strategy for green hydrogen production, extensive research has been conducted on photoelectrochemical (PEC) water splitting[1]. In order to activate the highly efficient solar energy conversion in the PEC cells, there are strong demands on resolving the sluggish kinetics of oxygen evolution reaction (OER) and ameliorating the poor conversion efficiency of the anode part for overcoming the energy barriers in the 4-electron steps of the water oxidation[2-5]. The performance of the PEC OER is determined by three fundamental factors: the light harvesting efficiency, which governs the number of photogenerated charge carriers; the charge transport efficiency, which encompasses the charge separation and collection processes including the critical aspect of charge recombination; and the charge transfer efficiency at the photoanode-electrolyte interface reaction sites[6-8]. In this context, n-type semiconductive transition metal oxides (TMO) have been explored as a potential photoanode material due to their cost-effectiveness, chemical stability, and suitable band alignment for the OER[9]. Among them, WO_3 stands out as a promising candidate for the highly active photoanode due to advantages such as an appropriate energy band structure with band gap energy, moderate hole diffusion length, and high electron mobility[10-15]. However, the practical application of the WO_3 faces challenges such as low charge transport efficiency due to deteriorated charge separation and collection by rapid charge recombination, low charge transfer efficiency resulting from poor surface OER kinetics, and instability caused by the defects-induced photo corrosion during the PEC operation in aqueous media[16,17]. Moreover, the PEC OER on the WO_3 photoanode in the neutral pH environment critically suffers from extremely poor surface reaction kinetics than in an acid condition due to the d-band center of WO_3 and its adsorption behavior of the intermediates during the 4-electron OER pathway[5,18-20]. Hence, improving the charge separation performance by suppressing the undesired recombination and enhancing the charge transfer efficiency to boost surface OER kinetics are critical for achieving the high efficiency of oxide-based PEC OER.

Among the various strategies to overcome the limitations of WO_3[21-24], doping of metal elements in the WO_3 nanostructure to produce a multi-metal oxide has been widely adopted since it is a facile process for improving the bulk properties of oxide photoanodes, where the charge carriers of the host material are increased by introducing heteroatoms from the doping process[25]. In general, doping can be categorized as *ex-situ* and *in-situ*, depending on whether the doping process is accompanied by the formation of the host material[26]. In the case of the *in-situ* doping, the fabrication process can be less complex than the *ex-situ* doping. However, the distributed dopants in the bulk of the host material may induce lattice distortion due to the size discrepancy between host atoms and dopants, acting as a charge recombination center[27-29]. Considering their obvious disadvantage, the *ex-situ* doping processes can be utilized as effective doping methods. Among the *ex-situ* doping methods, thermal diffusion-mediated doping is a facile and cost-effective approach for the doping of heteroatom metal elements into the TMO, but it suffers from prolonged annealing times and impurity injection control[30,31]. Furthermore, improving the surface OER kinetics remains a crucial challenge with the conventional thermal diffusion-mediated doping approach as it primarily focuses on bulk properties[32]. Therefore, a novel doping strategy that addresses the drawbacks associated with the conventional doping processes is necessary to achieve highly efficient PEC OER with WO_3.

Herein, we introduced dual doping of 2D nanoflake structured WO_3 with transition and post-transition metals using a facile ultrafast sol-flame doping strategy. The sol-flame doping can be performed by coating the dopant precursor in the form of sol and flame combustion treatment. Despite the short flame combustion process time for 40 s, the rapid thermal flux resulting from the high temperature of 1,000 °C introduced heteroatoms (Fe^{3+}) from the overlaid precursor and induced effective bidirectional dual doping into WO_3 by promoting the diffusion of Sn^{4+} derived from the fluorine-doped tin oxide (FTO) glass substrate without causing lattice distortion of the WO_3 or damaging the substrate. As a result, Fe and Sn co-doped WO_3 using sol-flame method (FL-doped WO_3) exhibited outstandingly enhanced thermodynamic charge transport efficiency and catalytic kinetics transfer efficiency of 83% and 76%, respectively, compared to those of 65% and 41%, respectively, for Fe-doped WO_3 using conventional thermal-mediated method (FN-doped WO_3) and 55% and 22%, respectively, for bare WO_3. Moreover, the charge recombination was effectively suppressed in the FL-doped WO_3 and the charge carrier lifetime was also prolonged compared to that of FN-doped WO_3 and bare WO_3. Consequently, FL-doped WO_3 achieved a significantly enhanced photocurrent density performance at 1.23 V_{RHE} in pH 7.0 aqueous electrolyte, which was 6.16 times higher than that of bare WO_3). Density functional theory (DFT) analysis confirms that the substitution doping of Fe and Sn atoms is induced on W sites. In addition, it reveals that Sn doping effectively improved charge transport efficiency and the co-doping of Fe and Sn enhanced surface OER kinetics of WO_3. Our research results propose a novel doping strategy beyond conventional methods. The flame doping strategy can maintain the structural stability of the semiconductor while facilitating dual transition metal atom co-doping, effectively improving charge transport efficiency and surface OER kinetics. We expect that our flame doping method can be applied to enhance PEC performance by extending it to various transition metal atom dopants and semiconductors.

EXPERIMENTAL

Fabrication of the bare WO_3 film

The bare WO_3 2D nanosheet structure was prepared on FTO glass (15 Ω) by using hydrothermal method. First, the WO_3 seed layer precursor was synthesized by adding 0.375 g of tungstic acid (99.9%, Sigma Aldrich) to 3 mL of hydrogen peroxide (H_2O_2, 30 wt%, Sigma Aldrich) and stirring at 140 °C until 1 mL of solution remained. Subsequently, the solution was dissolved in 9 mL deionized water (DI water) with 0.15 g of polyvinyl alcohol (70,000 M_W, MP Biomedicals) by stirring at 70 °C for 25 min. Then, the produced WO_3 seed solution was spin-coated (2,000 rpm, 30 s) onto FTO glass and annealed in a furnace at 500 °C for 2 h, repeating two times to obtain the WO_3 seed layer. Next, 0.179 g of tungstic acid was added to a mixed solution of 2.43 mL of H_2O_2 and 3.57 mL of DI water, and the mixture was stirred at 100 °C for 15 min to obtain the WO_3 precursor. Thereafter, 0.059 g of urea (99.0%, TCI), 0.024 g of anhydrous oxalic acid (99.0%, Sigma-Aldrich), 0.59 mL of 6 M HCl solution, and 14.84 mL of acetonitrile (99%, Acros Organics) were added sequentially to the 3.56 mL of pre-synthesized WO_3 precursor. After stirring for 10 min, the well-mixed solution was transferred to a 100 mL Teflon-lined stainless steel container with a WO_3 seed layer, stored at 180 °C for 2 h, and then the bare WO_3 photoanode was obtained after annealing at 500 °C for 2 h.

Fabrication of the FL-doped WO_3 and FN-doped WO_3

The FL-doped WO_3 (Fe and Sn co-doped WO_3 using sol-flame method) photoanode was synthesized through a sol-flame doping treatment. The Fe sol precursor was synthesized by adding 0.054 g of iron chloride hexahydrate (97%, Sigma Aldrich) and 33 μL of 6 M HCl to 20 mL of 2-metoxyethanol (99.8%, Sigma Aldrich) with 20 min stirring. Spin-coating was performed at 2,000 rpm for 40 s by dropping 150 μL of the synthesized Fe sol precursor onto bare WO_3. The flame doping experiment was carried out using a co-flow premixed flat flame burner (McKenna Burner). CH_4 and air were used as fuel and oxidizer. The flow rates of CH_4 and air were maintained at 2.22 and 21.1 standard liter per minute (SLPM), respectively. Then, the Fe sol-coated WO_3 was annealed directly in the flame for 40 s. After annealing, the WO_3 was

initially cooled on the upper side of flame for 30 s and then completely cooled in the air. For the FN-doped WO_3 (Fe-doped WO_3 using conventional thermal-mediated method), the same sol-coating process was implemented as with FL-doped WO_3. The sol-coated WO_3 was annealed in furnace at 500 °C for 30 min instead of the flame process to obtain FN-doped WO_3.

PEC measurements

All PEC tests were measured using the CHI instrument and Gamry 600+ workstation in electrolyte with a three-electrode cell configuration. Platinum wire and Ag/AgCl electrodes were selected as the counter and reference electrodes, respectively. The electrolyte was 0.1 M potassium phosphate (KPi) buffer solution (pH 7.0). A solar simulator (ABET Technologies Solar Simulators) was applied as an artificial sunlight source for 1 sun illumination (100 mW cm^{-2}). The 0.1 M KPi buffer solution with 0.5 M Na_2SO_3 was used as a hole scavenger (pH 7.74) to characterize the charge transport efficiency ($\eta_{transport} = J_{scavenger}/J_{abs}$) and the charge transfer efficiency ($\eta_{transfer} = J_{KPi}/J_{scavenger}$). Here, J_{abs} refers to the photon absorption rate expressed by the maximum charge density obtained from the light absorptance. Electrochemical impedance spectroscopy (EIS) tests were performed using a three-electrode configuration, with platinum wire and Ag/AgCl electrodes as the counter and reference electrodes, respectively. The analysis was conducted with an AC voltage amplitude of 5 mV across a frequency range of 1 MHz to 0.01 Hz at an applied bias potential of 1.23 V_{RHE} under simulated 1 sun illumination.

Photoluminescence and time-resolved photoluminescence measurements

The room-temperature photoluminescence (PL) spectra of WO_3 photoanodes were obtained using a fluorescence spectrophotometer (FS5, Edinburgh). The system was equilibrated for 2 h before measurements. An excitation source with a 350 nm wavelength was used to excite the sample and 395 nm of long-pass filter was used. The time-resolved PL measurement (TRPL) was conducted using a Nd:YAG-based pulsed laser system (Surelite II-10, Surelite), which generates the fundamental wavelength at 1,064 nm (1 W) with a repetition rate of 10 Hz and a pulse width of 4-6 ns, along with its second (532 nm) and third (355 nm) harmonics. The third harmonic (355 nm) was then separated using the Surelite Separation Package (SSP) and directed into an optical parametric oscillator (Surelite OPO, Surelite) to produce the 425 nm pump pulse used for excitation. After generating the 425 nm excitation pulse, the beam was directed onto the sample. The light reflected or emitted from the sample was then collected and guided along a beamline toward an ultrafast interferometer (GEMINI, NIREOS), which covers the spectral range of 230-2,300 nm. To remove stray laser light before detection, a 395 nm long-pass filter was placed in the beam path. The filtered signal was subsequently detected by an avalanche photodiode (C5658, Hamamatsu), and the resulting interferograms were recorded. By performing Fourier transforms of these interferograms, time-resolved spectral maps were obtained, providing insight into the PL dynamics of the sample.

Characterizations

The morphological properties and elemental mapping were evaluated by field emission scanning electron microscopy (FESEM, JSM-7600F) and high-resolution transmission electron microscopy (HRTEM, JEOL JEM-2000). X-ray diffraction (XRD, D8 ADVANCE with Cu Kα radiation) was utilized to determine the crystal structure and phase formation of the sample. Additionally, the chemical bonding between the constituent elements was determined by X-ray photoelectron spectroscopy (XPS, ESCALAB250). Raman measurements were performed using a RAMAN spectrometer (DXR2xi) equipped with 532 nm laser and an electron multiplying charge-coupled device (CCD) detector. Optical properties were identified using an ultraviolet-visible (UV-Vis) spectrophotometer (SHIMADZU UV-3600i plus).

RESULTS AND DISCUSSION

Morphological and compositional analysis

Fe element was utilized as dopants that effectively enhance the PEC performance of WO_3, taking advantage of their similarity in ionic radius to the host atom W^{6+} and their successful application in the n-type semiconductors[21,33,34]. Furthermore, we designed the co-doping for WO_3 with Fe and Sn, utilizing the phenomenon of Sn diffusion derived from FTO at high temperatures through a flame treatment[35]. The sol-flame doping methodology involves a two-step process: initial coating of the substrate with the dopant precursor in solution form (sol), followed by a controlled flame combustion treatment that facilitates rapid incorporation of dopant elements into the host structure. This approach enables efficient doping while maintaining the structural integrity of the material. The synthesis method of FL-doped WO_3 by the sol-flame method is illustrated in Figure 1A. The bare WO_3 was synthesized on the seed layer-coated FTO substrate by hydrothermal synthesis method, followed by spin-coating with Fe sol and flame treatment to fabricate FL-doped WO_3. In addition, to compare the FL-doped WO_3 with the conventionally doped WO_3, the FN-doped WO_3 was prepared by the thermal-mediated doping using a furnace. The images of the synthesized photoanodes are exhibited in Supplementary Figure 1. Scanning electron microscopy (SEM) images of the FL-doped WO_3 exhibit that the thin WO_3 nanoflakes were densely cross-linked to form a film with a thickness of 2 μm [Figure 1B and C]. The bare WO_3 and the FN-doped WO_3 showed no significant differences compared to the FL-doped WO_3. It indicates that the morphology and structure of WO_3 were not significantly affected by doping [Supplementary Figure 2]. In HRTEM measurements, the d-spacing (0.364 nm) of the typical monoclinic WO_3 (002) plane was observed in the FL-doped WO_3, FN-doped WO_3, and bare WO_3 [Figure 1D and Supplementary Figure 3]. After the doping process, Fe-based material from the Fe sol was barely observed in the HRTEM. HRTEM line profile analysis shows that Fe and Sn existed in the FL-doped WO_3 at 4.54% and 0.22% atomic percent, respectively[Figure 1E]. An inset figure in Figure 1E demonstrates that the detection of Sn. In addition, high-angle annular dark field (HADDF) and energy dispersive spectroscopy (EDS) mapping results validate the presence of Fe and Sn in FL-doped WO_3 [Figure 1F]. Due to the high-temperature thermal shock and cooling process in sol-flame method, the diffusion of the dopants to the thermodynamically stable position was promoted[36,37], which induced the uniform distribution of Fe and Sn elements.

Crystallinity analysis

To investigate the effect of doping on the crystallinity of WO_3, XRD patterns were measured. The three main peaks centered at $2\theta = 23.1^{\circ}$, 23.6°, and 24.3° represent the (002), (020), and (200) planes of monoclinic WO_3, respectively [Figure 2A]. The FL-doped WO_3 and FN-doped WO_3 exhibit monoclinic WO_3 peaks similar to the bare WO_3, indicating that additional heat treatment did not induce secondary phase formation of monoclinic WO_3 [Figure 2B]. Furthermore, the intensity of the peaks increased after the additional heat treatment for doping, suggesting that the enhanced crystallinity of WO_3 in the FL-doped WO_3 and FN-doped WO_3[38-42]. In particular, the rapid flame process effectively enhanced the crystallinity of WO_3 in the FL-doped WO_3 compared to the FN-doped WO_3 photoanode synthesized by the conventional doping process. However, unlike the FN-doped WO_3, the FL-doped WO_3 exhibited a significant increase in the signal of the (002) and (020) planes. These dominant facet changes in the FL-doped WO_3 are attributed to the reduction of short-distance structural disorder in WO_3 due to flame treatment[43-45]. On the other hand, the FN-doped WO_3 showed a similar peak tendency to the bare WO_3 and a decrease in the signal of the (002) plane. This is because the short-distance structural disorder was generated on the surface of the FN-doped WO_3 [Supplementary Figure 3]. The XRD data demonstrate that the high-temperature flame process preserves the intrinsic phase and enhances the crystallinity of the material, which affects the light harvesting efficiency, while allowing for effective doping.

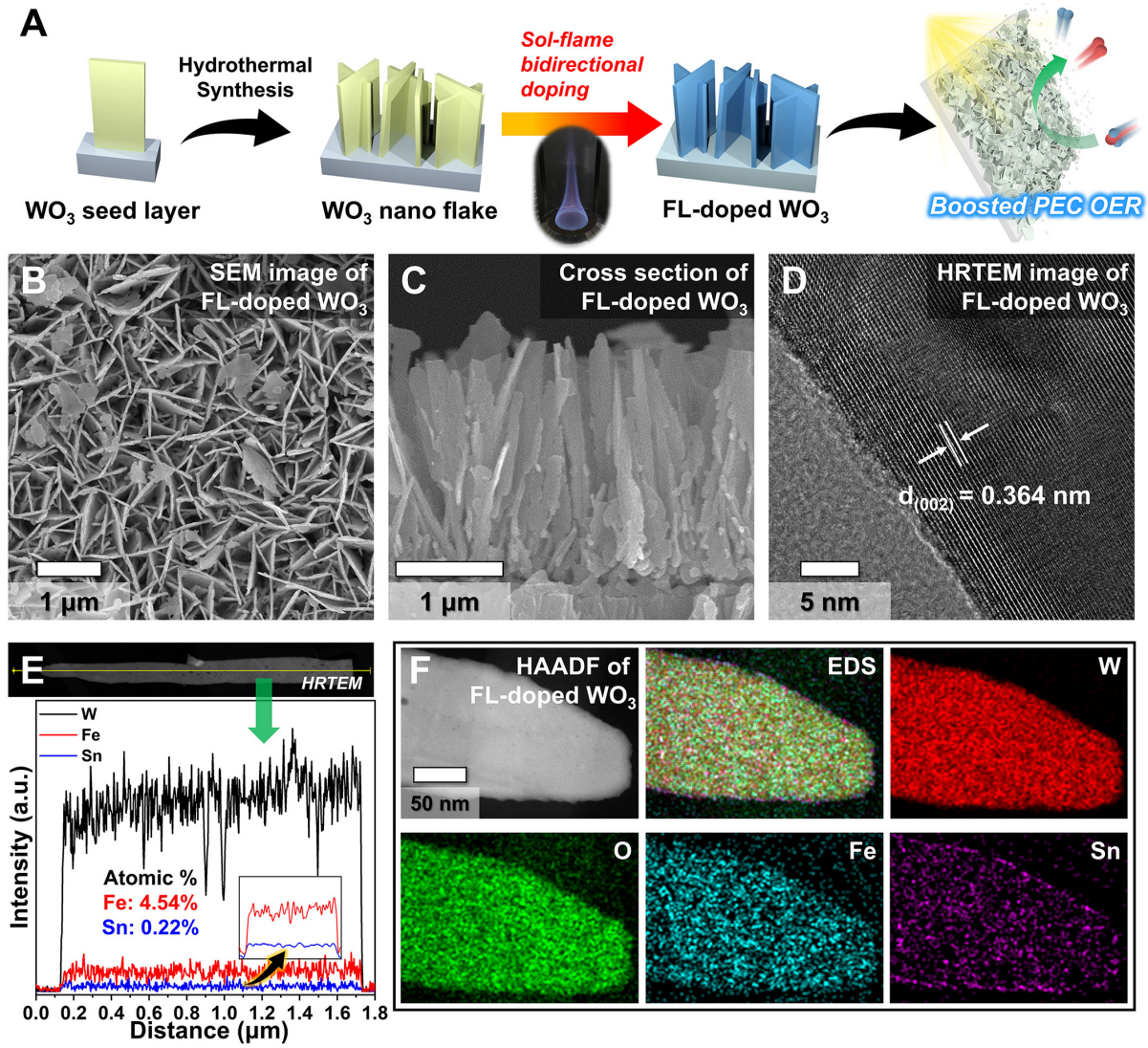

Figure 1. (A) Schematic illustration of the sol-flame doping method. (B) Top view and (C) cross section view of SEM images of the FL-doped WO_3. (D) HRTEM images of the FL-doped WO_3. (E) HRTEM line profile for the FL-doped WO_3. (F) HAADF image and EDS mapping for the FL-doped WO_3.

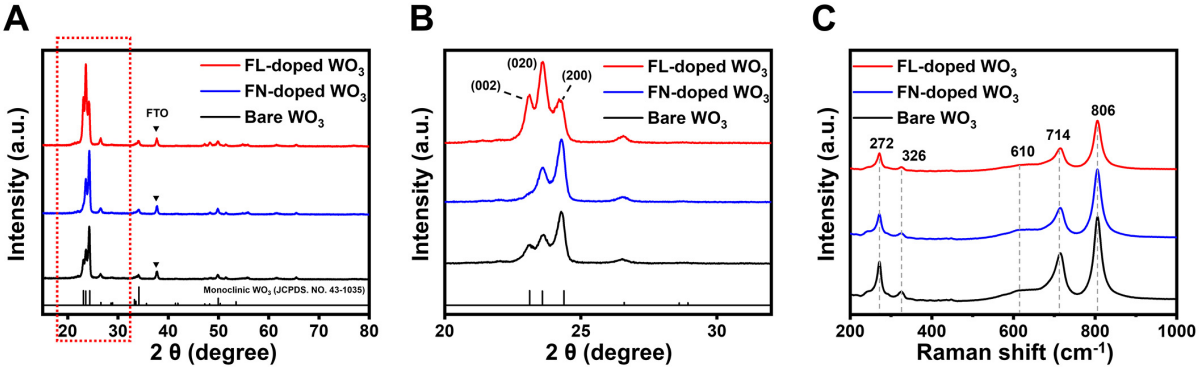

Figure 2. (A) XRD patterns of the FL-doped WO_3, FN-doped WO_3, and bare WO_3. (B) Enlarged XRD patterns on short range of 20°~32°. (C) Raman spectra of FL-doped WO_3, FN-doped WO_3, and bare WO_3.

Raman spectroscopy measurements were also performed to investigate the influence of doping on the local structure of WO_3 [Figure 2C]. The Raman band peaks centered at 272 and 326 cm^{-1} correspond to the bending modes of O-W-O, while the peaks centered at 714 and 806 cm^{-1} are related to the stretching modes of O-W-O[21,46]. No significant peak shift was observed in the FL-doped WO_3 and FN-doped WO_3 based on the bare WO_3. The intensity of the peak signal at 610 cm^{-1}, which is predicted to be residual hydrated WO_3, decreased with additional heat treatment[46,47]. The reduction in intensity of each O-W-O stretching and bending mode peak after doping is attributed to the substitution of W by the Fe dopants in the FN-doped WO_3, with a further decrease observed in the case of Fe and Sn co-doping in the FL-doped WO_3. The details of substitution doping are addressed further in the DFT section. The Raman data indicate that doping has no significant influence on the local structure of WO_3.

XPS analysis

XPS measurements were performed to investigate the surface chemical state of WO_3 after additional heat treatment and to further confirm the presence of dopants. No significant changes in the C 1s spectra, including the C-C bond at 284.8 eV, indicate that the flame process using CH_4 as a fuel was solely related to heat treatment and did not generate any by-products such as hydrocarbon materials on the surface [Supplementary Figure 4]. In the O 1s spectra, peaks corresponding to lattice oxygen (O_L), oxygen vacancy (O_v), and chemisorbed oxygen (O_c) appeared at 530.4, 531.5, and 532.8 eV, respectively, with no observable peak shift in FL-doped WO_3 and FN-doped WO_3 [Figure 3A]. The FL-doped WO_3 and FN-doped WO_3 exhibit reduced intensity in O_v and O_c compared to bare WO_3, indicating that additional heat treatment for doping reduced surface defects and removed residues. For W 4f, the FL-doped WO_3, FN-doped WO_3, and bare WO_3 exhibit the peaks of W^{6+} $4f_{7/2}$ and $4f_{5/2}$ centered at 35.3 and 37.5 eV, respectively, with no peak shift greater than 0.1 eV observed [Figure 3B]. Interestingly, the peaks of W^{5+} $4f_{7/2}$ and $4f_{5/2}$ centered at 34.2 and 36.2 eV in bare WO_3 disappeared in FL-doped WO_3 and FN-doped WO_3. This indicates that the intrinsic amorphous defects in the bare WO_3 were oxidized to become crystalline during heat treatment, which is consistent with the data showing reduced O_v in the XPS O 1s spectra and increased crystallinity signals in XRD[48]. The Fe 2p shown in Figure 3C demonstrates that Fe dopant existed on the surface of the doped WO_3. In the FL-doped WO_3 and FN-doped WO_3, Fe^{2+} $2p_{3/2}$ and Fe^{3+} $2p_{3/2}$ peaks appeared at 709.2 and 710.9 eV, respectively, while Fe^{2+} $2p_{1/2}$ and Fe^{3+} $2p_{1/2}$ peaks appeared at 723.1 and 724.8 eV, respectively. The Fe^{2+} signals in the FL-doped WO_3 and FN-doped WO_3 were mainly due to the presence of a small amount of FeO or Fe_3O_4 generated on the electrode surface during the doping process[49]. Especially in the FL-doped WO_3, an increased and sharpened signal of the Fe^{3+} was observed. It exhibits that the flame process effectively induced Fe^{3+} doping with less generation of oxidized Fe materials compared to the conventional doping method. In addition, Sn $3p_{3/2}$ peak centered at 716.4 eV in the Fe 2p spectra appeared only in the FL-doped WO_3, confirming that the co-doping by sol-flame occurred as intended. The presence of Sn doping in the FL-doped WO_3 can be further confirmed by Sn 3d XPS spectra, where Sn^{4+} $3d_{5/2}$ and Sn^{4+} $3d_{3/2}$ peaks appeared at 487.0 and 495.5 eV, respectively [Figure 3D]. In XPS valence band spectra, bare WO_3, FN-doped WO_3, and FL-doped WO_3 had an energy band gap of 2.42 eV between the Fermi level of the semiconductor (F_s) and the valence band edge [Supplementary Figure 5]. The comprehensive analysis, including SEM, TEM, Raman, and XPS clearly validates that the sol-flame doping strategy allows for efficient doping and co-doping than conventional doping method without damaging the physical properties of the material.

Photoelectrochemical performance

Linear sweep voltammetry (LSV) measurements were performed in 0.1 M KPi (pH 7) to investigate the enhancement of PEC OER performance in WO_3 by doping [Figure 4A]. The FL-doped WO_3 exhibited a significantly enhanced photocurrent density of 1.45 mA/cm^2, which is 6.16 times higher than the bare WO_3 with a photocurrent density of 0.24 mA/cm^2 at 1.23 V_{RHE}. The FL-doped WO_3 also outperformed the FN-

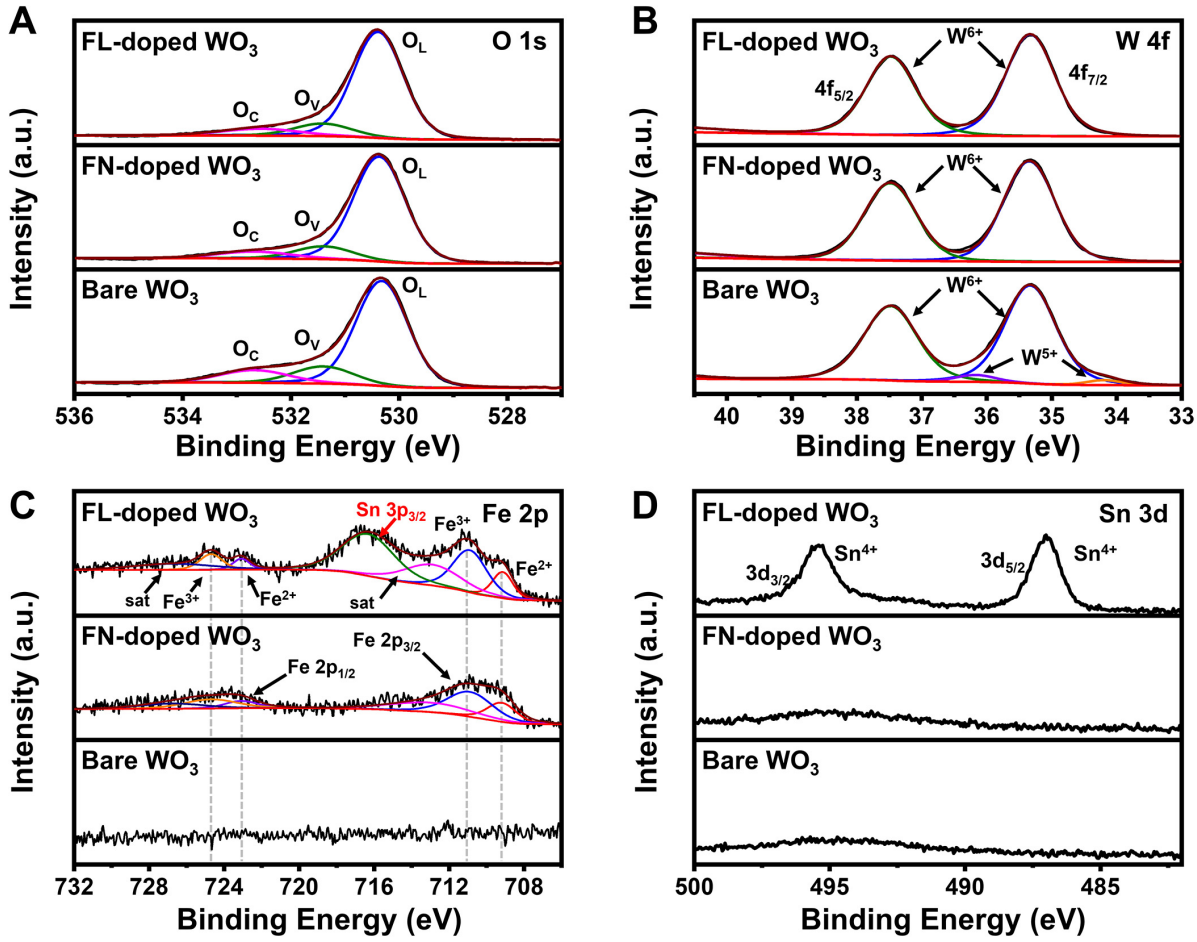

Figure 3. High-resolution XPS spectra of (A) O 1s, (B) W 4f, (C) Fe 2p and (D) Sn 3d for the FL-doped WO_3, FN-doped WO_3, and bare WO_3.

doped WO_3, which had a photocurrent density of 0.56 mA/cm^2 at 1.23 V_{RHE}. The same performance trend was observed in hole scavenger condition (pH 7.74) [Supplementary Figure 6]. The FL-doped WO_3, FN-doped WO_3, and bare WO_3 showed photocurrent densities of 1.85, 1.37, and 1.15 mA/cm^2, respectively, at 1.23 V_{RHE}. Also, applied bias photon-to-current efficiency (ABPE) measurements confirm that the FL-doped WO_3 can be efficiently operated in PEC OER [Supplementary Figure 7][50]. In order to analyze the factors contributing to the performance enhancement in detail, the light harvesting efficiency, charge transport efficiency ($\eta_{transport}$), and charge transfer efficiency ($\eta_{transfer}$), which influence the PEC OER performance, were examined. For light harvesting efficiency, absorptance (A) was derived from UV-vis measurements, which was calculated from the diffuse reflectance (R) and diffuse transmittance (T) of WO_3 electrodes (A = 100%-R-T) [Figure 4B, Supplementary Figure 8A and B]. In the wavelength region beyond 450 nm, where the energy is higher than the band gap of WO_3 electrodes, an increased light harvesting efficiency was observed for the FL-doped WO_3 and FN-doped WO_3 compared to the bare WO_3, which well supported the XRD analysis. In the longer wavelength region above 450 nm, the FL-doped WO_3 exhibited higher absorptance than the FN-doped WO_3, which had only Fe doping. It indicates that Sn dopant acts as a shallow donor in the FL-doped WO_3[21,51]. However, there was no significant change in the band gap [Supplementary Figure 8C]. In terms of the $\eta_{transport}$, the FL-doped WO_3 exhibited highest efficiency of 83% compared to the FN-doped WO_3 (65%) and bare WO_3 (55%) at 1.23 V_{RHE}, resulting from the co-doping of

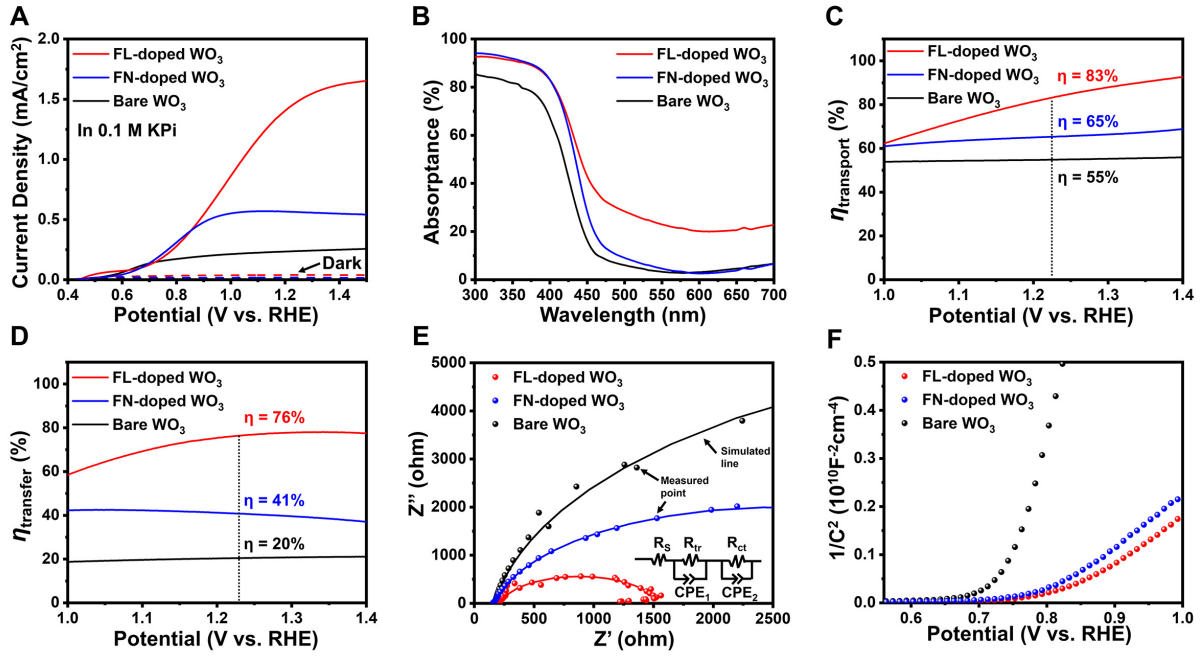

Figure 4. (A) PEC performance of WO_3 electrodes. (B) UV-vis absorptance spectra of WO_3 electrodes. (C) Charge transport efficiency and (D) charge transfer efficiency of WO_3 electrodes. (E) EIS (Electrochemical Impedance Spectroscopy) measurement of the WO_3 electrodes under 1 sun illumination (at 1.23 V *vs.* RHE, 10^6~0.01 Hz) and (F) Mott-Schottky plots of WO_3 electrodes.

Fe and Sn [Figure 4C]. Moreover, the FL-doped WO_3 exhibited a significantly improved $\eta_{transfer}$ of 76%, showing a more effective improvement from the bare WO_3 compared to FN-doped WO_3 (41%) [Figure 4D]. The doping process via post-heat treatment improved the crystallinity of WO_3, effectively enhancing the light harvesting efficiency, while simultaneously improving both $\eta_{transport}$ and $\eta_{transfer}$, with the Fe and Sn co-doped FL-doped WO_3 exhibiting the greatest improvements among all samples. These results demonstrate that dual-metal doping via the sol-flame method can be an effective strategy for enhancing PEC OER performance by ameliorating the aforementioned main factors: light harvesting efficiency, $\eta_{transport}$, and $\eta_{transfer}$.

In order to clarify the role of the dopants, additional investigations were carried out on Sn-doped WO_3, which was synthesized by the flame treated WO_3 without Fe sol (FL-treated WO_3, Supplementary Figure 9). XRD patterns of the FL-treated WO_3 showed an overall improved crystallinity similar to the FL-doped WO_3 and FN-doped WO_3 [Supplementary Figure 10]. The FL-treated WO_3 exhibited a weakened peak of the (002) plane, similar to the FN-doped WO_3. It indicates that both conventional doping and flame doping strategies result in a weakened (002) plane when doping with a single element regardless of species. XPS spectra of FL-treated WO_3 confirm the successful doping of Sn [Supplementary Figure 11]. The FL-treated WO_3 showed a photocurrent density of 1.09 mA/cm² at 1.23 V_{RHE} and increased absorptance compared to the bare WO_3 [Supplementary Figure 12]. The FL-treated WO_3 had a similar absorptance shape to the FL-doped WO_3, confirming that improving crystallinity through heat treatment enhances light harvesting efficiency and Sn dopant acts as a shallow donor. Therefore, the doping of Sn by the flame method efficiently improved the PEC OER, and the synergistic effect of Fe in the co-doping contributed to further boosting the performance by improving the $\eta_{transport}$ and $\eta_{transfer}$. EIS measurements were performed to gain further insight into the $\eta_{transport}$ and $\eta_{transfer}$ enhancements [Figure 4E]. Based on the circuit model presented in the inset figure, the simulated line was calculated from the measured data. The series resistance (R_s) at the electrode-substrate interface, the charge transport resistance within the electrode (R_{tr}), and the charge

transfer resistance at the electrolyte-electrode interface (R_{ct}) were derived from the simulation. The FL-doped WO_3 exhibited the lowest R_{tr} and R_{ct} values compared to the FN-doped WO_3 and bare WO_3, indicating enhanced $\eta_{transport}$ and boosted surface OER kinetics, suppressing the charge recombination. These results are well-matched with the $\eta_{transport}$ and $\eta_{transfer}$ data shown in Figure 4C and D. The fitted parameters are presented in Supplementary Table 1. Mott-Schottky plot of WO_3 electrodes is shown in Figure 4F, confirming an increase in donor density for the FL-doped WO_3 and FN-doped WO_3 after the doping process [Supplementary Table 2]. Moreover, the FL-doped WO_3 exhibits a higher donor density compared to the FN-doped WO_3, further validating the co-doping in the FL-doped WO_3, as supported by TEM and XPS analyses. Moreover, the stability test exhibited that the current retention of the FL-doped WO_3 was maintained for 24,000 s at the potential of maximum ABPE [Supplementary Figure 13].

Charge carrier dynamics

Furthermore, PL and TRPL measurements of WO_3 photoanodes were carried out to investigate the charge carrier dynamics [Figure 5]. As depicted in Figure 5A, the FL-doped WO_3 showed the most reduced PL intensity, following the FN-doped WO_3. It indicates that the charge recombination is effectively suppressed in doped WO_3, especially in the FL-doped WO_3[52,53]. This improvement tendency was also observed in TRPL results [Figure 5B]. The FL-doped WO_3 showed improved decay profile with prolonged photogenerated charge lifetime (7.48 ns) than FN-doped WO_3 (6.32 ns) and bare WO_3 (4.96 ns). The PL and TRPL results demonstrate that dual-metal doping by flame method effectively ameliorates the charge carrier dynamics, which contributes to the improvement of the charge transport efficiency. With the enhanced surface OER kinetics, the PEC OER performance of WO_3 is efficiently boosted. These enhancements are illustrated in Supplementary Figure 14 with a simplified energy band diagram.

DFT calculations investigations

To elucidate the performance enhancement when single Fe atoms and Sn, Fe co-doping are incorporated into WO_3, DFT calculations were conducted. Our prior characterizations confirmed that the FN-doped WO_3 involves simultaneous doping of Fe and Sn atoms, whereas the FL-doped WO_3 contains only Fe. Defect formation energy calculations were performed to investigate the doping sites of Fe and Sn atoms in the structure. To minimize periodic interaction errors and depict a dilute doping concentration, a 2 × 2 × 2 expanded supercell from the bulk WO_3 was utilized for structural modeling. Using the experimentally measured Fermi level, which is 2.42 eV away from the valence band maximum (VBM), as a reference point, the substitution of both Fe and Sn atoms for W atoms in WO_3 is determined to be thermodynamically most stable [Figure 6A and B, Supplementary Figure 5]. Consequently, all subsequent calculations hereafter considered substitutional doping.

Band structure calculations for the same 2 × 2 × 2 expanded supercell were then performed to probe the origins of increased $\eta_{transport}$ and improved electrical properties observed in electrochemical analysis. From Figure 3C, the higher intensity in FL-doped WO_3 compared to FN-doped WO_3 was observed, which indicates a higher amount of Fe atoms were introduced into the surface. Accordingly, one Fe atom was substituted in the FN-doped WO_3 supercell model, while in FL-doped WO_3, two Fe atoms and one Sn atom were substituted. In Figure 6C, bare WO_3 without doping exhibited flat bands near the VBM around the G k-path. However, doping with single Fe atom in FN-doped WO_3 [Supplementary Figure 15] and two Fe atoms and one Sn atom in FL-doped WO_3 resulted in parabolic bands. The widely recognized relationship states that the second derivative of curves in the band structure is inversely proportional to the effective mass, and reduction of effective mass directly enhances mobility, consequently influencing conductivity[54,55]. Thus, the co-doping of Fe and Sn atoms affected the hole effective mass near the valence band top, exhibiting improved hole mobility and conductivity beyond all models, explaining the enhanced $\eta_{transport}$.

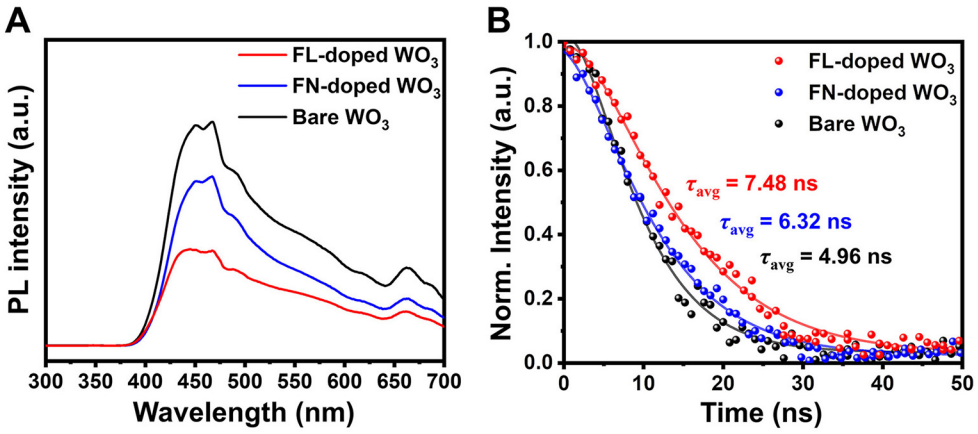

Figure 5. (A) PL intensities of FL-doped WO_3, FN-doped WO_3, and bare WO_3. (B) Normalized time-resolved photoluminescence (TRPL) of FL-doped WO_3, FN-doped WO_3, and bare WO_3. PL and TRPL were measured under room-temperature conditions. Detailed experimental information is provided in the experimental section.

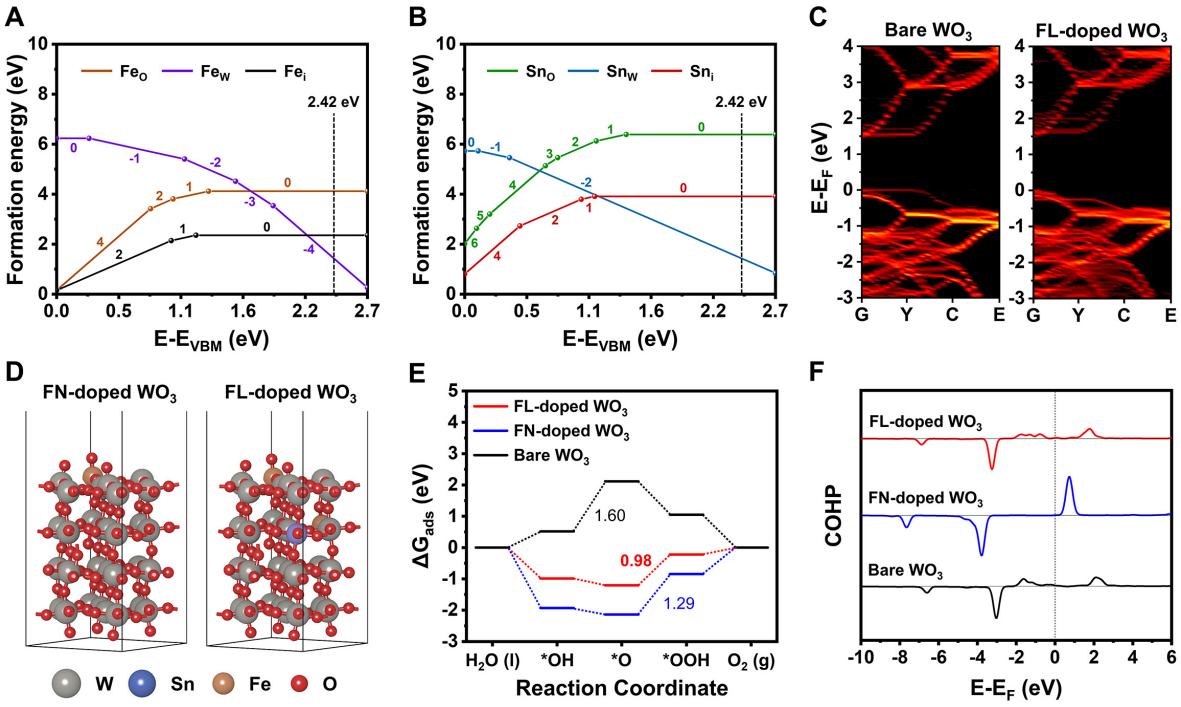

Figure 6. Defect formation energies of WO_3 for (A) Fe and (B) Sn. (C) Unfolded band structures for bare WO_3 and FL-doped WO_3. The letter G in x-axis denotes Γ k-path. (D) Geometry-optimized structures for FN-doped WO_3 and FL-doped WO_3. The grey, blue, ochre, and red spheres represent W, Sn, Fe, and O atoms, respectively. (E) Calculated OER landscape for bare WO_3, FN-doped WO_3, and FL-doped WO_3. (F) COHP results for bare WO_3, FN-doped WO_3, and FL-doped WO_3.

Next, surface modeling was conducted to calculate the OER kinetics. As previously mentioned, the structures of FN-doped WO_3 and FL-doped WO_3 were modeled through substitutional doping, as illustrated in Figure 6D. In Figure 6E, bare WO_3 exhibited weak adsorptions for all OER intermediates, with an overpotential of 1.60 eV, which is consistent with previous calculations[56,57]. In contrast, FN-doped WO_3 showed overall stronger adsorptions for all intermediates, and FL-doped WO_3, with the introduction of Sn atoms, exhibited an optimal adsorption strength compared to FN-doped WO_3. As a result, FL-doped WO_3

displayed an overpotential of 0.98 eV, making the OER kinetics more feasible compared to bare WO_3 (1.60 eV) and FN-doped WO_3 (1.29 eV). Similar trends were observed in the Crystal Orbital Hamilton Population (COHP) analysis [Figure 6F]. The regions above and below the horizontal line in each COHP plot represent anti-bonding and bonding states, respectively, with the Fermi level aligned to zero. Comparing bare WO_3 with FN-doped WO_3, the anti-bonding state below the Fermi level in FN-doped WO_3 decreased, and the overall energy window below the Fermi level penetrated deeper, indicating stronger bonding interaction with oxygen in FN-doped WO_3. On the other hand, FL-doped WO_3 exhibited less penetration than FN-doped WO_3, suggesting weakened bonding due to the presence of weak anti-bonding states below the Fermi level compared to FN-doped WO_3. Thereby, the co-doping of Fe and Sn in WO_3 photoanode improves the electrical characteristics and enhances the OER performance of FL-doped WO_3.

CONCLUSIONS

In summary, bidirectional dual-metal doping *via* facile flame doping method for enhancing the PEC performance of the WO_3 photoanode was demonstrated. In contrast to the conventional thermal-mediated doping method, the rapid thermal flux with flame treatment induced the doping of Fe element from the Fe precursor solution and the diffusion of Sn element from the FTO substrate, which enables the bidirectional co-doping of Fe and Sn on the WO_3 photoanode. XRD, XPS and Raman results confirmed that the flame treatment improved the crystallinity of the WO_3 without affecting the intrinsic phase and local structure during co-doping. As a result, the FL-doped WO_3 exhibited 6.16 times higher PEC OER performance compared to the bare WO_3 with a challenging amelioration of both photoinduced charge migration, surface water oxidation kinetics, charge recombination, and charge carrier lifetime by co-doping in neutral electrolyte condition. The DFT calculation demonstrated the enhancement of the electrical properties by lowering effective mass, and optimized adsorptions of OER intermediates. Our report provides an effective doping strategy to TMO photoanode for enhancing the PEC performance.

DECLARATIONS

Authors' contributions

Writing: Roh, S. H.; Kim, J.
Experimental analysis and investigation: Roh, S. H.; Kim, J.; So, W.; Li, Y.; Hong, W. T.; Kwon, H. M.
Validation: Jo, S. B.; Yang, W.; Oh, B. K.; Chung, C. H.; Park, J.
Review and editing: Ahn, C.; Kim, B. H.; Kim, J. K.
Supervision and project administration: Kim, J. K.

Availability of data and materials

Not applicable.

Financial support and sponsorship

This work was supported by the National Research Foundation of Korea (NRF) grant funded by the government of the Republic of Korea (MSIT) (No. RS-2024-00467234), and by the NRF grant funded by the Korean government (MSIT) (No. RS-2024-00405818).

Conflicts of interest

All authors declared that there are no conflicts of interest.

Ethical approval and consent to participate

Not applicable.

Consent for publication

Not applicable.

REFERENCES

1. Kim, J. H.; Hansora, D.; Sharma, P.; Jang, J. W.; Lee, J. S. Toward practical solar hydrogen production - an artificial photosynthetic leaf-to-farm challenge. *Chem. Soc. Rev.* **2019**, *48*, 1908-71. DOI PubMed
2. Rossmeisl, J.; Logadottir, A.; Nørskov, J. Electrolysis of water on (oxidized) metal surfaces. *Chem. Phys.* **2005**, *319*, 178-84. DOI
3. Man, I. C.; Su, H. Y.; Calle-Vallejo, F.; et al. Universality in oxygen evolution electrocatalysis on oxide surfaces. *ChemCatChem* **2011**, *3*, 1159-65. DOI
4. Song, J.; Wei, C.; Huang, Z. F.; et al. A review on fundamentals for designing oxygen evolution electrocatalysts. *Chem. Soc. Rev.* **2020**, *49*, 2196-214. DOI
5. Li, Y.; Je, M.; Kim, J.; et al. Rational nanopositioning of homogeneous amorphous phase on crystalline tungsten oxide for boosting solar water oxidation. *Chem. Eng. J.* **2022**, *438*, 135532. DOI
6. Jiang, C.; Moniz, S. J. A.; Wang, A.; Zhang, T.; Tang, J. Photoelectrochemical devices for solar water splitting - materials and challenges. *Chem. Soc. Rev.* **2017**, *46*, 4645-60. DOI PubMed
7. Yang, Y.; Niu, S.; Han, D.; Liu, T.; Wang, G.; Li, Y. Progress in developing metal oxide nanomaterials for photoelectrochemical water splitting. *Adv. Energy. Mater.* **2017**, *7*, 1700555. DOI
8. Klotz, D.; Grave, D. A.; Rothschild, A. Accurate determination of the charge transfer efficiency of photoanodes for solar water splitting. *Phys. Chem. Chem. Phys.* **2017**, *19*, 20383-92. DOI PubMed
9. He, H.; Liao, A.; Guo, W.; Luo, W.; Zhou, Y.; Zou, Z. State-of-the-art progress in the use of ternary metal oxides as photoelectrode materials for water splitting and organic synthesis. *Nano. Today.* **2019**, *28*, 100763. DOI
10. Wang, Y.; Tian, W.; Chen, C.; Xu, W.; Li, L. Tungsten trioxide nanostructures for photoelectrochemical water splitting: material engineering and charge carrier dynamic manipulation. *Adv. Funct. Mater.* **2019**, *29*, 1809036. DOI
11. Li, Y.; Mei, Q.; Liu, Z.; et al. Fluorine-doped iron oxyhydroxide cocatalyst: promotion on the WO_3 photoanode conducted photoelectrochemical water splitting. *Appl. Catal. B. Environ.* **2022**, *304*, 120995. DOI
12. Amano, F.; Tsushiro, K. Proton exchange membrane photoelectrochemical cell for water splitting under vapor feeding. *Energy. Mater.* **2024**, *4*, 400006. DOI
13. Huang, Y.; Li, J.; Wang, H.; et al. Candle-soot template-mediated synthesis of nanoporous WO_3 films as photoanodes for solar water splitting. *Appl. Mater. Today.* **2025**, *42*, 102553. DOI
14. Jafarpour, S.; Naghshara, H. Reactive co-sputter deposition of Ta-doped tungsten oxide thin films for water splitting application. *Sci. Rep.* **2025**, *15*, 8302. DOI PubMed PMC
15. Li, B.; Jiang, X.; Liang, T.; et al. WO_3 nanorod arrays decorated with isolated Fe active sites for photoelectrocatalytic water oxidation. *J. Colloid. Interface. Sci.* **2025**, *689*, 137257. DOI
16. Kim, W.; Tachikawa, T.; Monllor-Satoca, D.; Kim, H.; Majima, T.; Choi, W. Promoting water photooxidation on transparent WO_3 thin films using an alumina overlayer. *Energy. Environ. Sci.* **2013**, *6*, 3732. DOI
17. Zheng, G.; Wang, J.; Liu, H.; et al. Tungsten oxide nanostructures and nanocomposites for photoelectrochemical water splitting. *Nanoscale* **2019**, *11*, 18968-94. DOI
18. Li, Y.; Kim, M. C.; Xia, C.; et al. A natural molecule-driven organometallic conformal overlayer for high efficiency photoelectrochemical water splitting. *Appl. Catal. B. Environ.* **2024**, *343*, 123516. DOI
19. Shinde, P. A.; Jun, S. C. Review on recent progress in the development of tungsten oxide based electrodes for electrochemical energy storage. *ChemSusChem* **2020**, *13*, 11-38. DOI PubMed
20. Hill, J. C.; Choi, K. S. Effect of electrolytes on the selectivity and stability of n-type WO_3 photoelectrodes for use in solar water oxidation. *J. Phys. Chem. C.* **2012**, *116*, 7612-20. DOI
21. Song, H.; Li, Y.; Lou, Z.; et al. Synthesis of Fe-doped WO_3 nanostructures with high visible-light-driven photocatalytic activities. *Appl. Catal. B. Environ.* **2015**, *166-7*, 112-20. DOI
22. Wang, S.; Chen, H.; Gao, G.; et al. Synergistic crystal facet engineering and structural control of WO_3 films exhibiting unprecedented photoelectrochemical performance. *Nano. Energy.* **2016**, *24*, 94-102. DOI
23. Kim, J. H.; Yoon, J. W.; Kim, T. H.; et al. Heterostructure between WO_3 and metal organic framework-derived $BiVO_4$ nanoleaves for enhanced photoelectrochemical performances. *Chem. Eng. J.* **2021**, *425*, 131496. DOI
24. Seabold, J. A.; Choi, K. S. Effect of a cobalt-based oxygen evolution catalyst on the stability and the selectivity of photo-oxidation reactions of a WO_3 photoanode. *Chem. Mater.* **2011**, *23*, 1105-12. DOI
25. Parmar, K. P. S.; Kang, H. J.; Bist, A.; Dua, P.; Jang, J. S.; Lee, J. S. Photocatalytic and photoelectrochemical water oxidation over metal-doped monoclinic $BiVO_4$ photoanodes. *ChemSusChem* **2012**, *5*, 1926-34. DOI PubMed
26. Chen, B.; Ge, B.; Fu, S.; et al. Ex-situ flame co-doping of tin and tungsten ions in TiO_2 nanorod arrays for synergistic promotion of

solar water splitting. *Chem. Eng. Sci.* **2020**, *226*, 115843. DOI

27. Annamalai, A.; Shinde, P. S.; Jeon, T. H.; et al. Fabrication of superior α-Fe_2O_3 nanorod photoanodes through ex-situ Sn-doping for solar water splitting. *Solar. Energy. Mater. Solar. Cells.* **2016**, *144*, 247-55. DOI
28. Wang, G.; Ling, Y.; Li, Y. Oxygen-deficient metal oxide nanostructures for photoelectrochemical water oxidation and other applications. *Nanoscale* **2012**, *4*, 6682-91. DOI
29. Liu, Y.; Li, J.; Li, W.; et al. Electrochemical doping induced in situ homo-species for enhanced photoelectrochemical performance on WO_3 nanoparticles film photoelectrodes. *Electrochim. Acta.* **2016**, *210*, 251-60. DOI
30. Weigel, T.; Schipper, F.; Erickson, E. M.; Susai, F. A.; Markovsky, B.; Aurbach, D. Structural and electrochemical aspects of $LiNi_{0.8}Co_{0.1}Mn_{0.1}O_2$ cathode materials doped by various cations. *ACS. Energy. Lett.* **2019**, *4*, 508-16. DOI
31. Tang, L. B.; Liu, Y.; Wei, H.; et al. Boosting cell performance of $LiNi_{0.8}Co_{0.1}Mn_{0.1}O_2$ cathode material via structure design. *J. Energy. Chem.* **2021**, *55*, 114-23. DOI
32. Kim, J. H.; Lee, J. S. Elaborately modified $BiVO_4$ photoanodes for solar water splitting. *Adv. Mater.* **2019**, *31*, e1806938. DOI PubMed
33. Salem, M.; Akir, S.; Ghrib, T.; Daoudi, K.; Gaidi, M. Fe-doping effect on the photoelectrochemical properties enhancement of ZnO films. *J. Alloys. Compd.* **2016**, *685*, 107-13. DOI
34. Chakhari, W.; Ben, N. J.; Ben, T. S.; Ben, A. I.; Chtourou, R. Fe-doped TiO_2 nanorods with enhanced electrochemical properties as efficient photoanode materials. *J. Alloys. Compd.* **2017**, *708*, 862-70. DOI
35. Ling, Y.; Wang, G.; Wheeler, D. A.; Zhang, J. Z.; Li, Y. Sn-doped hematite nanostructures for photoelectrochemical water splitting. *Nano. Lett.* **2011**, *11*, 2119-25. DOI
36. Cho, I. S.; Lee, C. H.; Feng, Y.; et al. Codoping titanium dioxide nanowires with tungsten and carbon for enhanced photoelectrochemical performance. *Nat. Commun.* **2013**, *4*, 1723. DOI
37. Feng, Y.; Cho, I. S.; Cai, L.; Rao, P. M.; Zheng, X. Sol-flame synthesis of hybrid metal oxide nanowires. *Proc. Combust. Inst.* **2013**, *34*, 2179-86. DOI
38. He, Y.; Yan, Q.; Liu, X.; Dong, M.; Yang, J. Effect of annealing on the structure, morphology and photocatalytic activity of surface-fluorinated TiO_2 with dominant {001} facets. *J. Photochem. Photobiol. A. Chem.* **2020**, *393*, 112400. DOI
39. Trzciński, K.; Zarach, Z.; Szkoda, M.; Nowak, A. P.; Berent, K.; Sawczak, M. Controlling crystallites orientation and facet exposure for enhanced electrochemical properties of polycrystalline MoO_3 films. *Sci. Rep.* **2023**, *13*, 16668. DOI PubMed PMC
40. Wen, X.; Chen, C.; Lu, S.; et al. Vapor transport deposition of antimony selenide thin film solar cells with 7.6% efficiency. *Nat. Commun.* **2018**, *9*, 2179. DOI PubMed PMC
41. Antonaia, A.; Polichetti, T.; Addonizio, M.; Aprea, S.; Minarini, C.; Rubino, A. Structural and optical characterization of amorphous and crystalline evaporated WO_3 layers. *Thin. Solid. Films.* **1999**, *354*, 73-81. DOI
42. Feng, C.; Fu, S.; Wang, W.; Zhang, Y.; Bi, Y. High-crystalline and high-aspect-ratio hematite nanotube photoanode for efficient solar water splitting. *Appl. Catal. B. Environ.* **2019**, *257*, 117900. DOI
43. Li, Y.; Liu, Z.; Li, J.; Ruan, M.; Guo, Z. An effective strategy of constructing a multi-junction structure by integrating a heterojunction and a homojunction to promote the charge separation and transfer efficiency of WO_3. *J. Mater. Chem. A.* **2020**, *8*, 6256-67. DOI
44. Li, F.; Li, J.; Li, F.; et al. Facile regrowth of Mg-Fe_2O_3/P-Fe_2O_3 homojunction photoelectrode for efficient solar water oxidation. *J. Mater. Chem. A.* **2018**, *6*, 13412-8. DOI
45. Jang, J. W.; Du, C.; Ye, Y.; et al. Enabling unassisted solar water splitting by iron oxide and silicon. *Nat. Commun.* **2015**, *6*, 7447. DOI PubMed PMC
46. Santato, C.; Odziemkowski, M.; Ulmann, M.; Augustynski, J. Crystallographically oriented mesoporous WO_3 films: synthesis, characterization, and applications. *J. Am. Chem. Soc.* **2001**, *123*, 10639-49. DOI
47. Daniel, M.; Desbat, B.; Lassegues, J.; Gerand, B.; Figlarz, M. Infrared and Raman study of WO_3 tungsten trioxides and WO_3, xH_2O tungsten trioxide tydrates. *J. Solid. State. Chem.* **1987**, *67*, 235-47. DOI
48. Moulzolf, S. C.; Ding, S. A.; Lad, R. J. Stoichiometry and microstructure effects on tungsten oxide chemiresistive films. *Sens. Actuators. B. Chem.* **2001**, *77*, 375-82. DOI
49. Xia, C.; Li, Y.; Kim, H.; et al. A highly activated iron phosphate over-layer for enhancing photoelectrochemical ammonia decomposition. *J. Hazard. Mater.* **2021**, *408*, 124900. DOI
50. Kim, T. W.; Choi, K. S. Nanoporous $BiVO_4$ photoanodes with dual-layer oxygen evolution catalysts for solar water splitting. *Science* **2014**, *343*, 990-4. DOI PubMed
51. Kalanur, S. S. Structural, optical, band edge and enhanced photoelectrochemical water splitting properties of tin-doped WO_3. *Catalysts* **2019**, *9*, 456. DOI
52. He, Y.; Zhang, L.; Teng, B.; Fan, M. New application of Z-scheme Ag_3PO_4/g-C_3N_4 composite in converting CO_2 to fuel. *Environ. Sci. Technol.* **2015**, *49*, 649-56. DOI
53. Yan, L.; Dong, G.; Huang, X.; Zhang, Y.; Bi, Y. Unraveling oxygen vacancy changes of WO_3 photoanodes for promoting oxygen evolution reaction. *Appl. Catal. B. Environ.* **2024**, *345*, 123682. DOI
54. Silva, A. M.; Silva, B. P.; Sales, F. A. M.; et al. Optical absorption and DFT calculations in L -aspartic acid anhydrous crystals: charge carrier effective masses point to semiconducting behavior. *Phys. Rev. B.* **2012**, *86*, 195201. DOI
55. Wang, F.; Di Valentin, C.; Pacchioni, G. Electronic and structural properties of WO_3: a systematic hybrid DFT study. *J. Phys. Chem. C.* **2011**, *115*, 8345-53. DOI

56. Kishore, R.; Cao, X.; Zhang, X.; Bieberle-Hütter, A. Electrochemical water oxidation on WO_3 surfaces: a density functional theory study. *Catal. Today.* **2019**, *321-2*, 94-9. DOI
57. Shi, X.; Peng, H. J.; Hersbach, T. J. P.; et al. Efficient and stable acidic water oxidation enabled by low-concentration, high-valence iridium sites. *ACS. Energy. Lett.* **2022**, *7*, 2228-35. DOI